Delamination tests on CFRP-reinforced masonry pillars: Optical monitoring and mechanical modeling

R. Fedele [a,*], M. Scaioni [c], L. Barazzetti [b], G. Rosati [a], L. Biolzi [b]

[a] Department of Civil and Environmental Engineering (DICA), Politecnico di Milano, Piazza Leonardo da Vinci 32, 20133 Milan, Italy
[b] Department of Architecture and Building Constructions (ABC), Politecnico di Milano, Via Ponzio 31, 20133 Milan, Italy
[c] College of Surveying and Geo-Informatics, Tongji University, Siping Road 1239, Tumu Building B708, 200092 Shanghai, PR China

Received 29 January 2013
Received in revised form 21 July 2013
Accepted 9 October 2013
Available online 17 October 2013

1. Introduction

For the historical heritage and monumental buildings, possibly deteriorated by chemical–physical aging processes and past accidental events (such as earthquakes), there is a special need for retrofitting and repairing interventions. Fiber-Reinforced-Polymers (FRP), and especially those made of carbon fibers (CFRP), are available in the form of pultruded laminates, ready to be glued to the support, or possibly in multi-directional tissue to be embedded into grout and adhesive layers. Such reinforcements have been widely used in rehabilitation works for several reasons: (i) they exhibit excellent properties in terms of specific stiffness and strength, without increasing the structural mass; (ii) are extremely simple to apply and can adhere to differently shaped surfaces, even irregular or very rough; (iii) they turn out to be non-intrusive and non-destructive since exhibit low impact on the pre-existing scenario.

Delamination tests recently proposed for (C-)FRP reinforced masonry elements appear rather complex. Indeed they were conceived to avoid rigid body motions of the specimen whilst a tangential slip was applied between the reinforcement and the masonry support. The experimental campaigns performed so far have demonstrated that debonding usually occurs due to failure of masonry, see e.g. [5,12,19]. Also post-mortem observations showed that collapse mechanisms include a considerably thick layer of the underlying support.

It is worth emphasizing that such experiments suffer of intrinsic inaccuracies which are typical of civil engineering real-scale applications. They imply forces in the order of tons, causing deformation of the testing frame and connection elements, and may entail materials possibly derived from the historical heritage, that frequently feature irregular geometry, rough textures and inhomogeneities. For these circumstances, there is a special need of distinguishing structural effects, depending on the boundary conditions in the specific experimental set-up, from the constitutive, material response. Contact sensors, such as LVDTs and clip gauges, can provide high accuracy measurements but limited to a few control points on the specimen surface.

Recently, the use of digital cameras has enabled gathering enormous quantity of data at high space and time resolution. Such optical monitoring may concern tracking a specific group of pixels, suitably selected by the user (e.g. some points at the borders of

---

* Corresponding author. Tel.: +39 022399 4275; fax: +39 022399 4220.
E-mail address: roberto.fedele@polimi.it (R. Fedele).

cracks, as proposed in [2,3]). Alternatively, a dense field of displacements in 2D and 3D can be derived [11,18]. Possibly, recourse can be made to artificial textures generated by sprayed paintings, markers or projected patterns of interferometric fringes. Indeed, the first basic problem in optical monitoring is how to look for the corresponding features in two different images, which is addressed to as Digital Image Correlation (DIC). Several image matching techniques have been developed to obtain this goal, as reviewed in [15]. As the features are tracked in the two-dimensional (2D) image space, the second problem concerns how to derive metric information in the object space that in general is a 3D environment.

Basically, digital images can be considered as projective transformations of real objects, after proper corrections to compensate for some secondary effects like lens distortion. The parameterization of transformation models can be developed on the basis of different approaches (purely algebraic, or based on physically meaningful parameters). However, the projective transformation can be simplified if the shape of the monitored surface is roughly flat and in-plane displacements turn out to be predominant. In this situation one image acquired by a single fixed camera is strictly sufficient to extract metric information, because the object space reduces to a 2D space. On the other hand, in the more general situation including a truly 3D-shaped surface, the above approximation does not hold and at least two synchronized cameras must be adopted. Three dimensional coordinates can be derived from spatial intersection of rays projecting corresponding features. The higher is the number of cameras covering the same Region-Of-Interest, the better will be the precision and reliability of the results (see [13,18]).

In this context, simple and accurate numerical tools are required for optimizing the restoration design on structural elements, to predict their nonlinear response under conditions which are difficult to recreate in laboratory. In fact, damage processes occurring inside a masonry pillar, especially at the interface between quasi-brittle constituents and external reinforcements, are expected to govern the overall behavior at collapse, see e.g. [8–10].

The case-study here proposed, with reference to a CFRP reinforced masonry pillar subjected to single-lap shear test, shows the important capabilities of a synergistic approach combining conventional overall data (reaction force and stroke), with point sensors (LVDTs and clip gauge), non-conventional measurements techniques (namely, single camera 2D Digital Image Correlation) and advanced finite element models.

The paper is organized as follows. The experimental test, with details on the selected materials and the specimen preparation, is described in Section 2, with special emphasis on optical monitoring and provisions herein implemented for the error assessment. Section 3 is devoted to the three-dimensional finite element model developed under the hypothesis of perfect adhesion. In Section 4, experimental data are critically and comparatively assessed at the light of computer simulations and no-contact, kinematic full field measurements provided by 2D Digital Image Correlation. Closing remarks and future prospects are outlined in Section 5.

Notation: In what follows, the acronyms ROI and DIC will denote the Region-Of-Interest and the 2D (plane) Digital Image Correlation procedure, respectively. Symbols h_j indicate homography parameters, not to be confused with the damage model softening function h. S.I. units (namely [mm], [N], and then [MPa]) will be used throughout the paper, although for practical reasons different engineering units can be seldom preferred, namely: the centimeter [cm] for lengths at the macro-scale; the metric ton [t] or *tonne* unit, equivalent to 1000 kg and to approximately 9.81 kN.

2. Shear tests and full field measurements

2.1. Materials, specimen preparation and testing machine

The masonry pillar considered in this study was made of three historical clay bricks derived from a XVII century rural building. Each one of them had slightly irregular sides of size approximately 29 × 6.7 × 12.5 cm (width × height × depth), and were connected by two mortar joints, with 2.7 cm average thickness (see Fig. 1). The resulting anchor length of the CFRP strip (5.5 cm wide) amounted to 15 cm, and an initial notch (not glued) of 5 cm was present.

Inside the pillar, joints were realized by a high strength certified mortar. The unusual thickness of the mortar joints cushions the irregular profile of the historical bricks and corresponds to the current state-of-the-art in the restoration interventions on ancient and monumental buildings. The initial reinforcement strip consisted of a "four directional" texture (a patented commercial product), with a 0.1 mm nominal thickness, which was subjected to a rigorous preparation protocol. Indeed, after polishing the support surface (by means of compressed air jet), the following steps were accomplished: (i) one primer layer was applied by a roller on the specimen surface; (ii) another grout coat was daubed by a trowel, well compacted and levelled; (iii) finally, three layers of epoxy adhesive interspersed by two identical CFRP layers were accurately superimposed with the aid of a paintbrush. About 30 days were required as curing period, along which shrinkage and hardening can develop. The free end of the CFRP strip, to be fastened to the loading machine, was glued by a high resistance adhesive (at temperature 80 °C) to two thin blocks of a glass fiber laminate, and finally fixed into two bolted steel plates.

For the experimental tests, an electro-mechanical testing machine (Instron 8562) with 100 kN maximum capacity was used. Figs. 1 and 2 provide pictures and a simplified scheme of the tested sample and the adopted experimental set-up, respectively. The masonry pillar was fixed by means of a stiffened steel frame, designed to reduce as much as possible rigid body motions. The free end of the CFRP strip was clamped within two bolted steel plates (Fig. 2), and fixed above to the testing machine frame through pinned connections. During the shear test, the relative displacement between the CFRP reinforcement and the masonry pillar, usually referred to as (overall) tangential slip, was enforced by the actuator stroke at the frame basis (see Fig. 2).

Local values of the relative tangential displacement between the CFRP external reinforcement and the masonry support were monitored by conventional contact point sensors, namely by two inductive LVDTs and a resistive clip gauge (see detail in Fig. 2). In fact two LVDTs with a reference basis of about 5 cm (i.e. the monitored distance) were located symmetrically with respect to the CFRP strip, closely to the notch in the upper part of the monitored surface. The clip gauge, located at the reinforcement anchorage in the lower part of the pillar, provided the feed-back signal (0.4 μm/s speed was assumed) for the closed-loop test control with integral and derivative gain, in order to capture the response of the reinforced pillar up to complete debonding of the external CFRP strip. The experimental data are critically and comparatively discussed in Section 4.

2.2. Optical monitoring

To accurately detect the in-plane displacement field of the specimen outer surface (where the reinforcement is located), recourse was made to no-contact, kinematic full-field measurements by a 2D DIC algorithm. During the shear test, a sequence of digital images were acquired by a Nikon D80 digital camera (sensor with

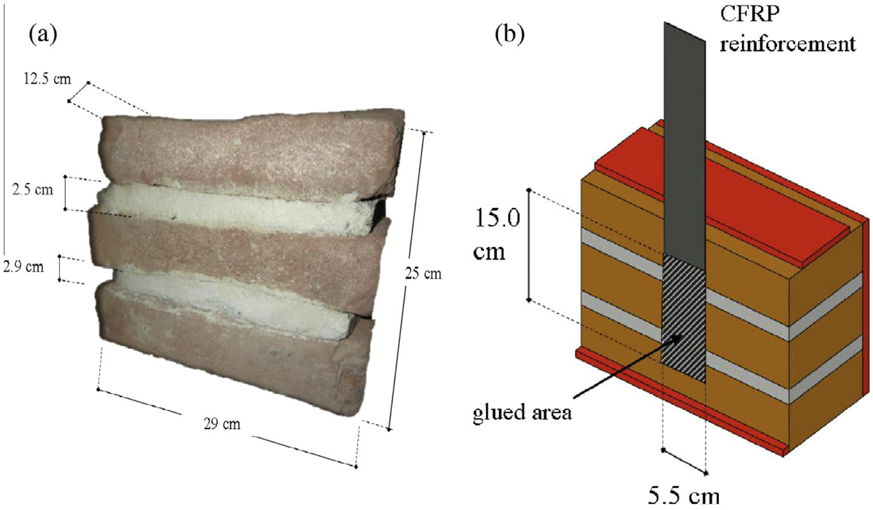

Fig. 1. Masonry pillar constituted of three historical clay bricks (XVII century), bonded by two joints of high strength mortar: main quotes are shown in (a), while idealized geometry with the external CFRP reinforcement in (b).

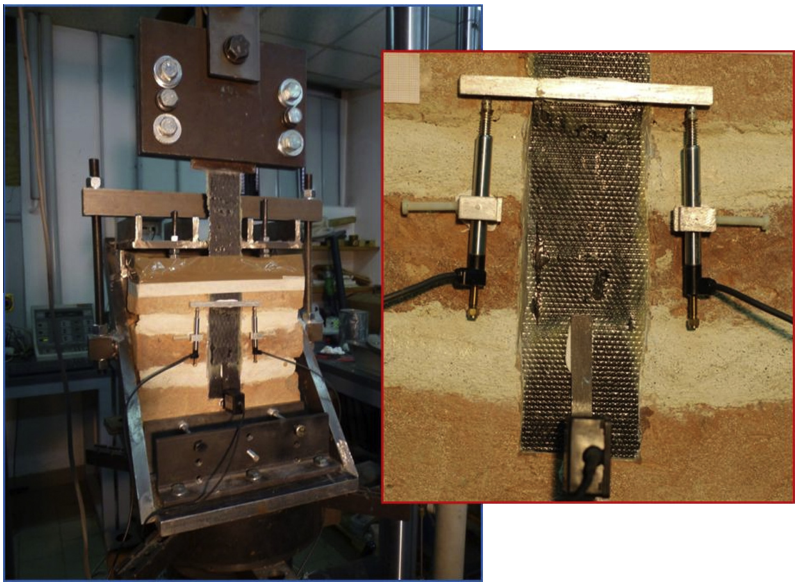

Fig. 2. The testing frame stiffened by diagonal connecting rods, including the reinforced masonry pillar. In the close-up window a detail of the monitored surface is shown, equipped with two LVDTs and a clip gauge.

$n_W \times n_H = 3872 \times 2592$ pixels, pixel size $p_z = 6.1$ µm, 12-bit RAW digitalization, Sigma lens with focal length $l_f = 50$ mm/F1.8 maximum aperture). The camera was placed on a stable photographic tripod, with the sensor approximately parallel to the specimen surface. Artificial lighting resulted in even illumination of the object.

The application of 2D DIC procedure was intended to detect the dense displacement field throughout the monitored specimen surface, starting from a reference initial state. In addition to the DIC features already highlighted in Section 1, herein it is worth emphasizing that an accurate mathematical model is needed to map points from the image space to the object space. From a conceptual standpoint, such a model is constituted of two different ingredients: (a) a quantitative description to compensate for optical distortion of a specific camera; (b) a rigorous geometric transformation to take into account the imperfect parallelism between the sensor plane and the flat object.

(a) Image distortions due to optical lens are unavoidable, although these could be significantly reduced by means of special provisions (e.g. by using a long focal length). The relevant correction procedure for a generic camera is usually referred to in the jargon as camera intrinsic calibration. To this purpose recourse was made to a suitably parameterized mathematical relationship, apt to describe the most typical image distortions, as schematically outlined in Fig. 3. Usually, calibration of a consumer-grade digital camera is accomplished by using the relationship proposed by Brown [17], governed by the following eight parameters: the principal distance (usually very close to the focal length l_f), the principal point offset (ξ_p, η_p), three coefficients (k_1,k_2,k_3) to compensate for radial symmetric distortion, and other two coefficients (p_1,p_2) for decentering distortion. The estimation of Brown parameters can be performed by a standard photogrammetric procedure, before the camera is used for the experiment, and on the basis of several digital pictures of ad hoc designed calibration frame [14].

Once that camera calibration parameters were estimated, the coordinates of suitably identified control points in the image space

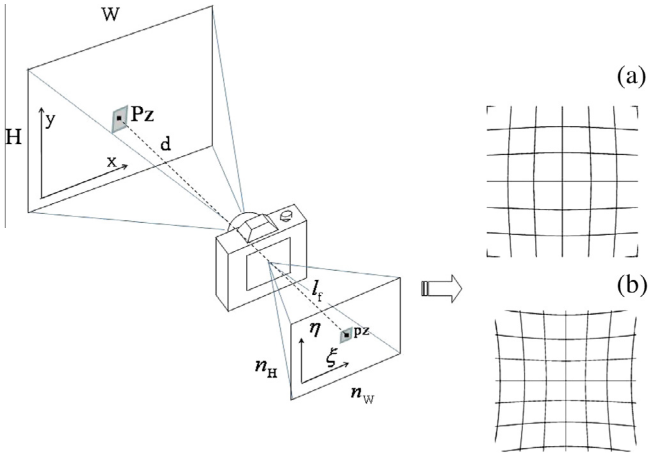

Fig. 3. Projective map between the image space and the object space: under coplanarity assumption, it is governed by parameters d, l_f and p_z; in the general case, by a complete 8-term homography. Main types of lens distorsions are schematically indicated at the right side, namely barrel in (a) and pincushion in (b).

(ξ, η) could be corrected obtaining calibrated image coordinates (ξ', η') as follows:

$$\begin{aligned} \xi' &= \xi_p + \xi^*(k_1 r^2 + k_2 r^4 + k_3 r^6) + p_1(r^2 + 2\xi^{*2}) + 2p_2\xi^*\eta^* \\ \eta' &= \eta_p + \eta^*(k_1 r^2 + k_2 r^4 + k_3 r^6) + p_2(r^2 + 2\eta^{*2}) + 2p_1\xi^*\eta^* \end{aligned} \tag{1}$$

where $\xi^* = \xi - \xi_p$ and $\eta^* = \eta - \eta_p$ are the image coordinates referred to the *principal point*, and $r^2 = \xi^{*2} + \eta^{*2}$ the Euclidean distance from it.

In Eq. (1) the prevalent error component is usually due to radial distortion, described by the truncated power expansion inside the first parenthesis. Consequently, the areas corresponding to the image corners feature the largest errors, while the central part of the image has almost nil deformations. It is worth emphasizing that herein we are looking for displacements, namely for a difference in point coordinates. When a point remains in the same region of the image, this kind of error will be negligible. In the present application, the worst scenario would lead major errors of about 3 pixels, namely of approximately 0.250 mm in the object space. This error is small also because of the good quality of the adopted lens, the moderately long focal length (50 mm), and the proximity of the camera to the object. The major errors would occur for a point moving from the center of the image up to the corners, with a displacement magnitude exceeding 190 mm. In the present experiment, maximum displacements amounted only to a few mm. However, camera calibration correction was applied because such errors are not homogeneous over the image, and because of the high precision of DIC procedure assessed by benchmarking tests (see later).

(b) In the experiment, flatness of the monitored specimen surface suggested the adoption of a rigorous 2D ↔ 2D projective transformation, usually referred to as homography [16]. In the truly reasonable hypothesis that the camera was stable during the experiment, a unique homography could be used to transform the calibrated image coordinates (ξ', η') of a control point (properly identified in the pictures) into the object space (X, Y), as follows:

$$X = \frac{h_1\xi' + h_2\eta' + h_3}{h_7\xi' + h_8\eta' + 1}, \quad Y = \frac{h_4\xi' + h_5\eta' + h_6}{h_7\xi' + h_8\eta' + 1} \tag{2}$$

The eight homography parameters ($h_j, j = 1, \ldots, 8$) can be worked out with a minimum of four control points, which can be identified with high accuracy in both image and object space. To this aim, a so-called registration frame, including a set of thirteen control points, was overlapped to the sample exclusively at the initial reference state. Control points consisted in circular marks (see Fig. 4), whose centers, although distorted, can be accurately measured in the images by means of a least-square image matching algorithm, see [18]. In the ideal conditions accuracy on the target's coordinates of approximately ±0.05 p_z can be achieved. The corresponding object coordinates of control points must be independently measured, e.g. by applying a fully 3D photogrammetric survey.

In synthesis, the following steps were implemented: (i) identification of the pixel coordinates of each control point belonging to the registration frame; (ii) correction of the image coordinates of control points to obtain their calibrated image coordinates by Eq. (1); (iii) least-square estimate of the homography parameters (h_j) based on Eq. (2). After steps (i)–(iii), any point from the image space can be transformed into the object space by a closed-form procedure, i.e. the operational product of Eqs. (1) and (2).

It is worth emphasizing that grayscale intensity values of digital images gathered during the test were not altered. In fact, the computation of piece-wise constant displacement fields was carried out by using a standard 2D DIC procedure performed on the original image sequence. In particular, normalized cross-correlation was used as a matching metric between image pairs, see e.g. [17]. The correlation code applied in this study, entirely developed in a Matlab® environment, is based on a reiterated application of Fast Fourier Transform (FFT), with reference to small pixel blocks (in the jargon referred to as templates) extracted from the ROI. The results directly obtained from FFT application were refined by polynomial interpolation, allowing for sub-pixel accuracy on the estimated displacements of about 0.1 p_z, depending however on a large extent on the surface texture and the overall image quality. DIC results achieved on the basis of the original images were corrected a posteriori by applying Eqs. (1) and (2) to the current

Fig. 4. Validation of optical monitoring system in the laboratory, by means of a dual-axis slide (with accuracy ±10 μm) and a registration frame with control points.

coordinates of the pixel block centroids, in order to reduce the inaccuracies of types (a) and (b) above outlined.

2.2.1. Design of the acquisition set-up

If the coplanarity condition between the sensor and object surface is roughly met, some basic rules can be adopted to assess the acquisition set-up. Indeed, under such assumption only three parameters govern the acquisition stage: the pixel size of the sensor (or pitch, p_z), the focal length of the lens (l_f), and the average distance from camera to object (d). These parameters turn out to vary significantly from case to case, since they depend on the adopted camera, the selected lens, and the optical set-up, respectively. The average pixel footprint on the object (P_z) and the image coverage ($W \times H$) can be consistently reckoned by looking at the scheme in Fig. 3, as follows:

$$P_z = p_z \frac{d}{l_f}, \quad W = P_z \cdot n_W, \quad H = P_z \cdot n_H \tag{3}$$

Quantity P_z affects the image resolution, whilst W and H allow one to assess whether the selected ROI is included in the camera field-of-view. For the experiment under study, design parameters were as follows: $p_z = 6.1$ μm, $l_f = 50$ mm, $d = 686$ mm, $n_W = 3872$, and $n_H = 2592$. These resulted in $P_z = 0.084$ mm, $W = 324$ mm, and $H = 217$ mm.

In a similar way, also the out-of-plane thickness ($\delta = 2$ mm) of the registration frame affected the homography parameters governing Eq. (2), since control points are slightly in relief from the specimen surface and closer to the camera. Under the coplanarity condition, the actual displacement s was underestimated by a factor λ, namely:

$$s = s' \cdot \lambda = s' \cdot \left(1 + \frac{\delta}{l_f} \frac{p_z}{P_z}\right) \tag{4}$$

being s' the computed displacement.

Herein a maximum value $\lambda = 1.003$ was estimated, implying an error of about 0.3% on the displacement magnitude, which was retained not meaningful for the present study.

2.2.2. Benchmarking the optical monitoring system

A preliminary assessment of the optical monitoring procedure was accomplished by the strategy proposed in [2]. As shown in Fig. 4, a masonry brick with a rough natural texture was located on a dual-axes slide. Here (rigid body) displacements with accuracy of ±10 μm can be independently prescribed along two directions. As shown in Fig. 4, a registration frame was carefully placed onto the specimen (the same to be adopted later for shear tests). The aim of these tests was to assess the overall system precision also by estimating out-of-plane scale factor λ through Eq. (4), disregarding approximations to be done later in a more complex scenario. Six independent sets of displacements were prescribed to the masonry brick, then the average trajectory of points tracked with DIC was compared to the given steps and discrepancies worked out. Generally, the mean value of discrepancies in each series was not statistically significant. The Root Mean Square Error (RMSE) of all tests was purely based on the standard deviation of measurements, i.e. on their random scatter, and the residuals resulted approximately Gaussian with a vanishing bias. A value of RMSE = 15.9 μm was found, i.e. equal to 0.19 P_z when compared to the footprint of the pixel size on the object. This outcome included both the uncertainty of the homography estimation and the unresolved residuals in the image matching process, and it was affected also by the intrinsic uncertainty of the slide positioning. By extrapolating these estimates to the real experiment set-up, a 95%-confidence interval of about ±31.2 μm on displacement estimates is ideally achievable.

3. Test simulation by finite elements

The delamination response of the reinforced masonry pillar was simulated in a finite element approach by an advanced three dimensional heterogeneous model. Only the key features of the adopted model are outlined in what follows, whilst reference is given to [6,7] for further details.

The quasi-brittle response of the constituent materials (brick and mortar) was described herein as elastic-damageable, then derivable through differentiation from a free energy Helmholtz potential. The following stress–strain relationship was adopted:

$$\boldsymbol{\sigma} = 2\mu(1 - D)\mathbf{e} + K(1 - D)tr\,\boldsymbol{\varepsilon}\mathbf{1} \tag{5}$$

where symbols $\boldsymbol{\sigma}, \boldsymbol{\varepsilon}, \mathbf{e} \equiv \boldsymbol{\varepsilon} - (tr\,\boldsymbol{\varepsilon}/3)\mathbf{1}$ denote the stress, strain and deviatoric strain tensor, respectively, being $tr\,\boldsymbol{\varepsilon} = \varepsilon_{ij}\delta_{ij}$ and $\mathbf{1} = \delta_{ij}$ the trace and the second-order identity operator, respectively; symbol D indicates the equivalent isotropic damage variable, affecting both the shear and bulk elastic moduli, denoted by symbols $\mu = G \equiv E/[2(1+\nu)]$ and $K \equiv E/[3(1-2\nu)]$, respectively. Overall damage is here conceived as the result of two possible damaging mechanisms, one for the states of prevailing tension and the other for compression, associated to different scalar damage variables, namely $D \equiv 1 - (1 - D_t) \cdot (1 - D_c)$. The evolution of such damage variables is governed by the following loading–unloading conditions:

$$f_t \leqslant 0 \quad \dot{D}_t \geqslant 0 \quad f_t\dot{D}_t = 0 \quad f_c \leqslant 0 \quad \dot{D}_c \geqslant 0 \quad f_c\dot{D}_c = 0 \tag{6}$$

where f_t and f_c are two activation functions, for the stress states of prevailing tension and compression, respectively, defined in the stress space as follows:

$$\begin{aligned} f_t(\boldsymbol{\sigma}, D_t, D_c) &= J_2 - a_t I_1^2 + b_t h_t I_1 - k_t h_t^2 \\ f_c(\boldsymbol{\sigma}, D_t, D_c) &= J_2 + a_c I_1^2 + b_c h_c I_1 - k_c h_c^2 \end{aligned} \tag{7}$$

In the above equation, symbols exhibit the following meaning: $I_1 = tr\boldsymbol{\sigma}$ denotes the first invariant of the stress tensor, $J_2 = 1/2 s_{ij}s_{ji}$ the second invariant of the stress deviator $\mathbf{s} \equiv \boldsymbol{\sigma} - (tr\,\boldsymbol{\sigma}/3)\mathbf{1}$, whereas a_t, b_t, k_t and a_c, b_c, k_c are non negative material parameters; h_t and h_c are isotropic hardening–softening functions to be defined later.

The current elastic domain is then defined in the stress space by the inequalities $f_t \leqslant 0\hslash$ and $f_c \leqslant 0$. The geometric locus with implicit equation $f_t = 0$ corresponds to a branch of a hyperboloid in the principal stress space, while $f_c = 0$ defines an ellipsoid. Both hyperboloid and ellipsoid are aligned with the hydrostatic axis, i.e. the trisectrix of the first octant with equation $\sigma_\xi = \sigma_\eta = \sigma_\zeta$, being σ_i ($i = \xi, \eta, \zeta$) the principal stresses. The shape and position in the stress space of these geometrical figures depend on parameters a_t, b_t, k_t, a_c, b_c, k_c which have to satisfy consistency conditions, as specified in [6].

The evolution of the elastic domain with damage variables is governed by the hardening/softening functions h_t and h_c defined as follows (being $i = c$ or t, for compression and tension, respectively):

$$h_i(D_i) = \begin{cases} 1 - (1 - \sigma_{ei}/\sigma_{0i})(1 - D_i/D_{0i})^2 & D_i < D_{0i} \\ \left[1 - \left(\frac{D_i - D_{0i}}{1 - D_{0i}}\right)^{m_i}\right]^{0.75} & D_i \geqslant D_{0i} \end{cases} \tag{8}$$

Symbol σ_{ei}/σ_{0i} denotes the ratio between the stresses at the elastic limit and at the peak, respectively, in uniaxial tension ($i = t$) or compression ($i = c$) test; D_{0i} is the damage level corresponding to the peak stress in the same uniaxial test; m_i is the material parameter governing the negative slope of the softening branch of the functions $h_i(D_i)$. The damage model outlined above has been

Table 1
Damage model parameters adopted for the historical bricks and high-strength mortar joints.

Model parameter	Meaning	Brick	Mortar
E	Young modulus	4250 MPa	5000 MPa
ν	Poisson ratio	0.1	0.1
a_t	Parameter governing tensile damage activation function f_t	0.329	0.12
b_t	Parameter governing tensile damage activation function f_t	3.78 MPa	2.4 MPa
k_t	Parameter governing tensile damage activation function f_t	6.2 MPa^2	10.5 MPa^2
$(\sigma_{et}/\sigma_{0t})$	Uniaxial stress at the elastic limit/uniaxial peak stress, in tension	0.8	0.8
D_{0t}	Tensile damage at peak	0.1	0.1
a_c	Parameter governing compressive damage activation function f_c	0.0025	0.0025
b_c	Parameter governing compressive damage activation function f_c	2.75 MPa	1.1 MPa
k_c	Parameter governing compressive damage activation function f_c	36 MPa^2	28 MPa^2
$(\sigma_{ec}/\sigma_{0c})$	Uniaxial stress at the elastic limit/uniaxial peak stress, in compression.	0.7	0.7
D_{0c}	Compressive damage at peak	0.3	0.3
G_t	Fracture energy in tension	0.14 N/mm	0.09 N/mm
G_c	Fracture energy in compression	14 N/mm	9 N/mm

implemented in the commercial finite element code ABAQUS, through a Fortran User-defined MATerial subroutine (VUMAT), see [1].

The above parameters entering Eqs. (7)–(8) were estimated on the basis of additional experimental tests performed by the authors on historical bricks, and of the producer information for mortar and CFRP strips. However, these information were further integrated by literature data (see e.g. [4]). Rigorous mathematical formulae provided in [6] allow one to relate the material strengths for the engineering practice to the model parameters which do not possess a clear physical meaning. Model parameters assumed for computer simulations are outlined in Table 1, and relevant elastic domains under plane stress conditions are drawn in the Haigh-Westergaard principal stress space in Fig. 5, for both brick and mortar materials.

The adopted finite element discretization of the tested pillar is shown in Fig. 6. This model includes ideal (i.e. non-compliant) constraints to prevent rigid body motions, consistently with the experimental set-up: the simulation was driven by a monotonically increasing displacement (referred to as overall tangential slip), prescribed to the reinforcement free end as boundary condition. As a simplified hypothesis, perfect adhesion was assumed between the elastic reinforcement and the damageable masonry support: in fact, damage processes occurring inside the bulk material were expected to be predominant with respect to the elastic slips of intermediate layers constituting the final reinforcement.

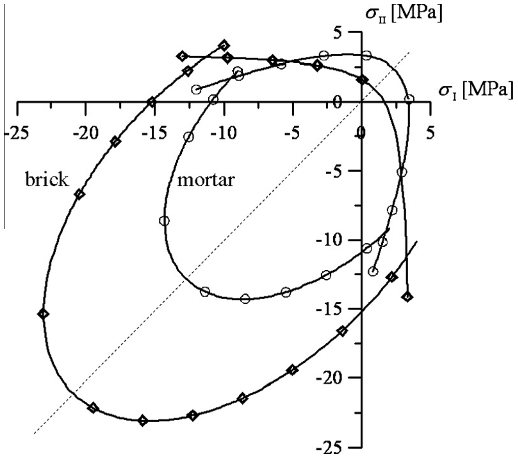

Fig. 5. Initial elastic domain under plane stress conditions, in the Haigh-Westergard principal stress space, adopted for computer simulations: historical brick (line marked by rhombs) and high strength mortar (marked by circles).

For the test simulation an explicit integration scheme was adopted, although conditionally stable. The time integration step was about one millionth of the whole test duration, in terms of final tangential displacement (or its rate) prescribed to the reinforcement. The kinetic energy was continuously monitored and it remained confined to a negligible percentage (less than 1%) of

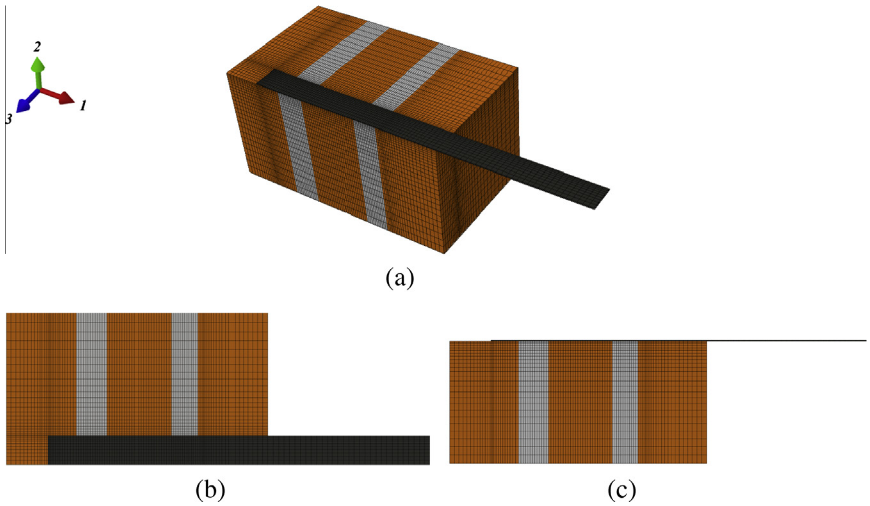

(a)

(b)

(c)

Fig. 6. Three-dimensional finite element model of the reinforced pillar (due to the symmetry, only one half of the specimen was discretized): (a) axonometric view; (b) upside view of the plane (1,3); (c) lateral view of the plane (1,2).

the overall strain energy cumulated by the specimen. A simple but effective regularization strategy based on the characteristic length was used to reduce mesh dependency. By the above procedure, local parameter m_i in Eq. (8) was updated in order to let constant the fracture energy dissipated at each integration point, independently from the element size. The interested reader is forwarded to [9,10] for further details.

3.1. DIC estimation of reinforcement elastic modulus

In situ kinematic measurements provided by DIC during the shear test were used to estimate the effective (or apparent) Young modulus of the CFRP reinforcement, in combination with the overall reaction force. As explained in Section 2, according to the preparation protocol two CFRP strips were embedded into several layers of adhesive suitably superimposed and subjected to curing. The macroscopic stiffness of the final reinforcement turns out to be far from the nominal value provided by the producer (concerning exclusively the original CFRP tissue and equal to 230 GPa). Displacements estimated by DIC concerned a small region in the upper part of the CFRP reinforcement, not glued to the support (i.e. located above the notch). Effective elastic modulus along the loading direction resulted $E_{CFRP} = 36.2$ GPa. Such modulus could also be provided by the 'mixture rule' when considering for the original CFRP strips a percentage transversal section of about 15% (corroborated by visual inspection), and attributing to the remaining section area the adhesive nominal stiffness of 1.4 GPa.

4. Comparative assessment of delamination response

As briefly mentioned in Section 2, the single-lap shear test was performed under clip-gauge control. Stroke was selected as control variable exclusively at the beginning of the experiment, when clip displacement at the CFRP attachment resulted small. Fig. 7 shows the overall reaction force as a function of the actuator displacement (or stroke), in (a), of the displacements provided by LVDTs (actually, their average) and by the clip gauge in (b) and (c), respectively. As expected, the history of the actuator stroke does not correspond to the relative tangential displacements between the CFRP and the masonry pillar experienced by the specimen, since the former is affected by both the overall machine stiffness and the deformability of the steel frame. On the basis of such results, the following considerations are made.

A marked snap-back behavior can be observed in Fig. 7(a) (between instants II and III), where the variable running along the abscissae axis is the actuator stroke. In principle, this behavior might be considered not so unusual, due to the elastic energy released by the specimen after strain localization and by the testing machine frame. Obviously, the clip displacement, selected as feedback signal for the test control, monotonically increases during the experiment and no snap-back is observed along the force versus clip plot Fig. 7(b). Surprisingly, in Fig. 7(c) where the LVDT signal is considered, snap-back behavior appears again (for clarity, the average of the two gauges is plotted).

Actually, the snap-back phenomenon in Fig. 7(c) (between instants II and III) has to be regarded as a consequence of an in-depth crack opening inside the lowest brick, closely to the CFRP attachment (see Fig. 8). This is probably due to pre-existing flaws in the historical clay material. Accordingly, also the snap-back behavior resulting in Fig. 7(a) was presumably emphasized. Due to such unexpected crack, with a typical wedge shape, the relative displacement detected by the clip exceeds significantly the LVDT measurements (of about 1 mm). In particular, when the reaction force decreases to about 3.5 kN (Fig. 7), the clip displacement equals the LVDT datum (around 150 µm), and, after that instant, progressively increases.

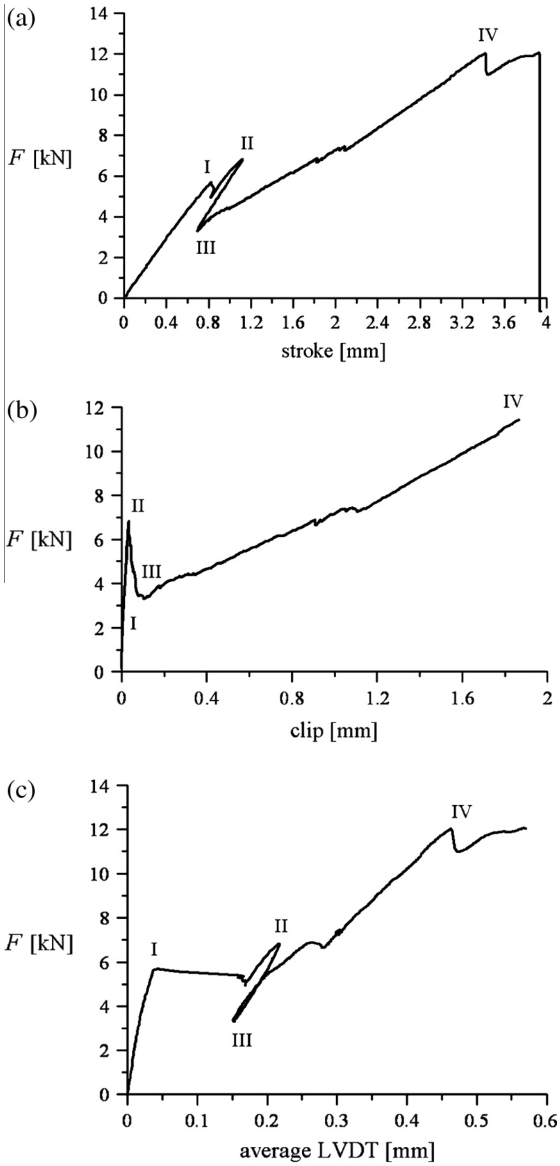

Fig. 7. Reaction force F during the single-lap shear test as a function of: (a) actuator stroke; (b) relative displacement provided by the clip gauge, at the CFRP strip attachment, adopted as feed-back signal for the test control; (c) mean value of two LVDTs at the notch, symmetrically located with respect to the reinforcement axis. Snap-back response can be observed not only in (a), but even in (c). Main phases of the test are also schematized: I, delamination onset; I → II, debonding along the first mortar joint; II → III: sudden unloading due to last brick cracking; III → IV, debonding propagation along the second brick and mortar joint; IV, onset of the spoon-shaped bulk mechanism closely to the CFRP anchorage.

In Fig. 7(c) it is rather interesting to observe the presence of a wide plateau, along which the reaction force is almost constant with respect to the LVDT displacement (between instants I and II). Such plateau corresponds to a small jump along the force versus stroke plot, see Fig. 7(a), localized at the end of the initial linear branch, before the above mentioned snap-back ring. An analogous phenomenon is repeated closely to the force peak in Fig. 7(a) and (c).

The response of the masonry pillar during the test can be understood in depth through a critical comparison of conventional experimental information with kinematic full-field measurements

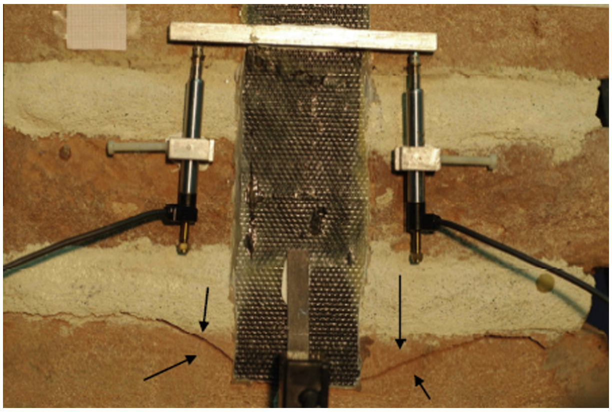

Fig. 8. In-depth crack emerging at the monitored surface during the test, favored by pre-existing flaws in the historical bricks.

and advanced finite element simulations. As a matter of fact, the novel mortar herein used for the unusually wide joints, characterized by rather high stiffness and strength, has ensured an almost complete bonding of pillar joints during the test, but it has determined also unexpected stress concentrations inside the historical bricks.

As a first step, a cross validation between full-field measurements and point sensor data is considered. The agreement observed in Fig. 9 between point data (clip gauge and LVDTs) and the relevant DIC estimates is indeed noteworthy, also at the light of some circumstances outlined in what follows. To perform a comparison between punctual and 'diffuse' sensors, DIC displacements were averaged over small regions closely to the reference points of LVDT bases but not exactly at the same locations (which obviously in digital images are covered by the sensor). The same procedure was applied for the clip gage datum. Of course, these 'geometric' errors affecting the DIC-estimated displacements cannot be removed. Moreover, in the present configuration LVDT data were affected by small rotations of the contrast bar, glued to the reinforcement (see Fig. 9). In fact, propagation of delamination front was herein endowed by a non-uniform deformation of the reinforcement, due to the irregular brick geometry, the rough texture of the support, and to the presence of several grout and glue layers that were superimposed in situ. Therefore, the unresolved residuals in Fig. 9 between the DIC estimates and point sensor output do not weaken but in a sense corroborate the present methodology.

The three-dimensional finite element analyses indicate that damage processes develop not only closely to CFRP–masonry interface, but also in the brick volume, leading to non-trivial bulk mechanisms responsible for the overall collapse. Fig. 10 shows contour maps of damage in tension variable D_t at different loading steps during the test simulation. Along the initial branch of the overall force versus slip plot, at the loading phase labeled as *a*, the presence of damage can be recognized over the first mortar joint, closely to the notch. At the subsequent instant labeled as *b*, damage begins to develop closely to the CFRP–masonry interface, over the (second) brick. Just after that instant, looking at the overall response a small knee can be distinguished: it indicates that the current crack front has surpassed the first mortar joint, followed by complete debonding. A contour map of damage inside the pillar at instant *b* helps us to explain the presence of the plateau in Fig. 7(c), corresponding to the sudden jump with a small loading decrease in Fig. 7(a).

At the subsequent loading phase *d*, when the current delamination front is surpassing the second mortar joint, the damage path along the CFRP-support interface does not increase, whereas a

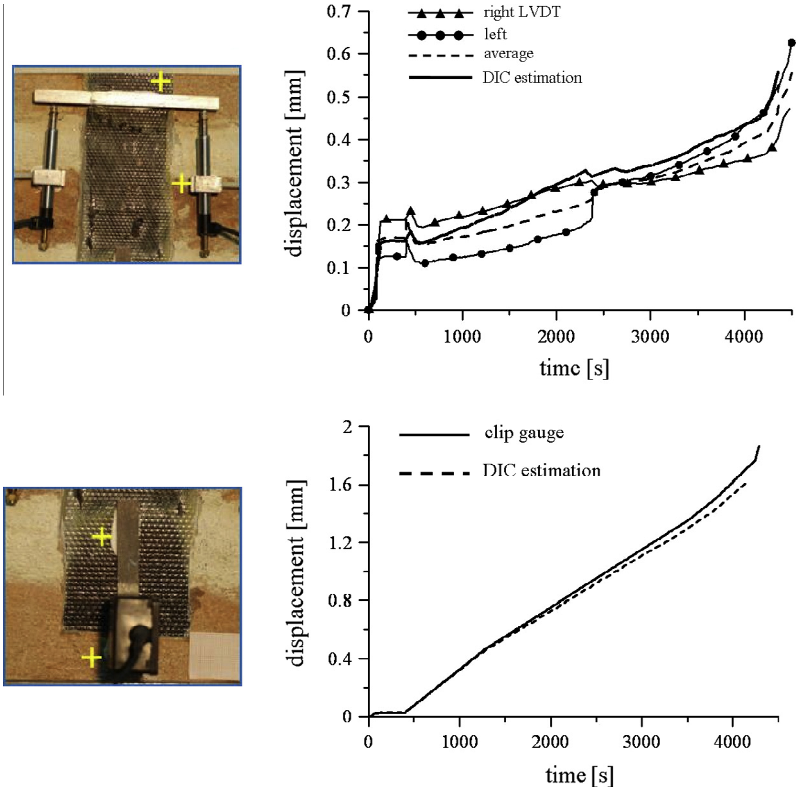

Fig. 9. Measurements provided by contact point sensors (LVDTs and clip gauge) and relevant DIC estimates, versus the experiment time. Inside the picture column at the left side, crosses indicate centroids of regions over which absolute displacements were detected by DIC and averaged.

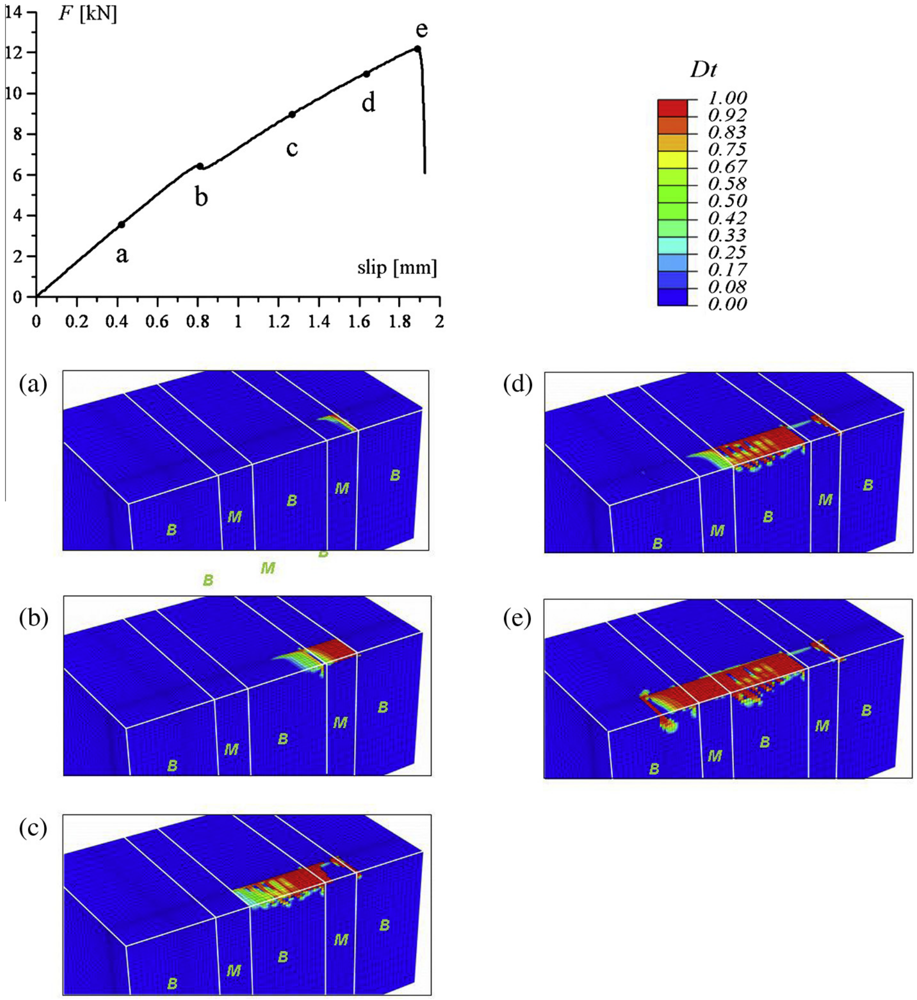

Fig. 10. Finite element simulation of the shear test: evolution of damage in tension D_t inside the pillar, at measurement instants a–e. Symbols *B* and *M* denote brick and mortar materials, respectively, whilst CFRP strip has been removed from the plot.

curved branch at the reinforcement attachment appears. The initiation of a bulb-shaped mechanism can be observed in Fig. 10(e): it occurs as soon as the current delamination front approaches the FRP attachment, at a distance of one half of the entire reinforcement width (about 3 cm). Under such scenario the applied force acting on the outer reinforcement, no longer balanced by bonding tractions over the first part of the joint, induces stress concentration at the FRP anchorage (in the last brick), and rapidly tensile damage begins to develop inside. This circumstance clearly demonstrates that the mechanical interaction at the masonry–reinforcement interface cannot be described by means of point springs with no mutual coupling.

From a mechanical standpoint, due to the presence of quasi-brittle constituents inside the pillar, these phenomena can be interpreted as bifurcations along the loading path. At the beginning, the direction of this secondary crack branch developing at the FRP attachment is approximately orthogonal to the interface: therefore, locally mode I (peel) loading conditions are met. Under a further increment of the overall tangential slip, mixed mode conditions cause the crack to deviate along a curved trajectory. Simultaneously, also at the second brick damage propagates inside the bulk material.

During the transition from *d* to *e*, a significant enlargement of the bulb can be noticed, with damage developing in-depth and also laterally inside the last brick. Unfortunately, the adopted explicit simulation does not allow one to follow in a stable way the entire bulb formation. At the last brick, the damage path along the interface, previously abandoned in favor of the curved branch of the bulb, is soon re-activated. Under a further increase of overall tangential slip it propagates dynamically along the CFRP-support interface, causing the final collapse endowed by a peak of kinetic energy. Simultaneously, a spoon-shaped damage mechanism develops also inside the second brick, in the middle of the pillar. Damage contours at instants *d* and *e* allow to explain the second sudden decrease of loading noticed in Fig. 7(a) and (c), closely to the force peak (instant IV).

Fig. 11 shows the distribution of tensile damage computed by the finite element model at collapse, drawn on the deformed configuration of the masonry pillar. Post-mortem analysis of the detached reinforcement (see Fig. 12) confirmed the presence of bulb-shaped material glued to the reinforcement, markedly thicker over the second brick (in the middle): the outer contour turns out to be in excellent agreement with the numerical predictions, as showed in the lower detail of Fig. 11. The mortar layers (white colored) still glued to the reinforcement are almost negligible: also this circumstance is in agreement with the finite element analyses, predicting damage along the mortar joints almost exclusively limited to the interface.

To compare in a consistent fashion the experimental response (clip-controlled) with the numerical simulations, the ‘actual’ history of overall tangential slip was reconstructed through DIC procedure. To this purpose, since the CFRP free end was fixed to the

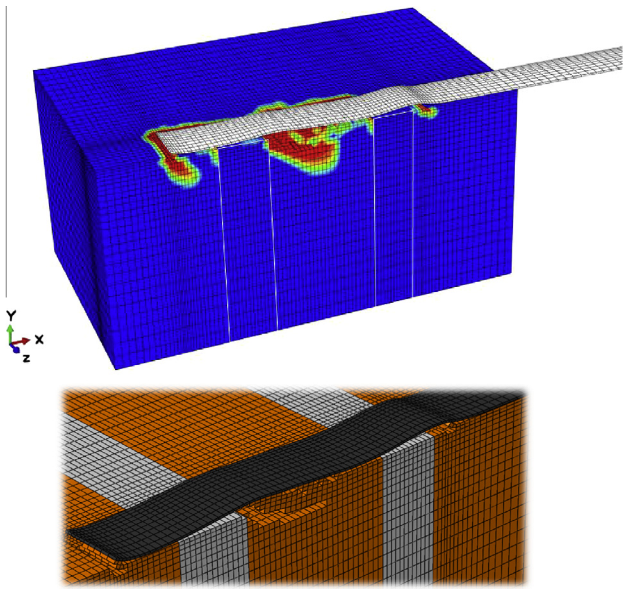

Fig. 11. Predictions of finite element analysis at collapse: distribution of damage in tension D_t inside the masonry pillar, drawn on the magnified deformed shape, and a detail closely to the reinforcement, illustrating the collapse mechanism. Finite elements in which damage variable exceeded a suitable threshold (close to unity), were eliminated from the analysis and eroded in the plot. Deformed shape is magnified ten times.

Fig. 12. Post-mortem pictures of masonry pillar and detached reinforcement. Part of the support is still glued to the CFRP strip, thicker in the middle (over the second brick), and indicates the bulk collapse mechanism.

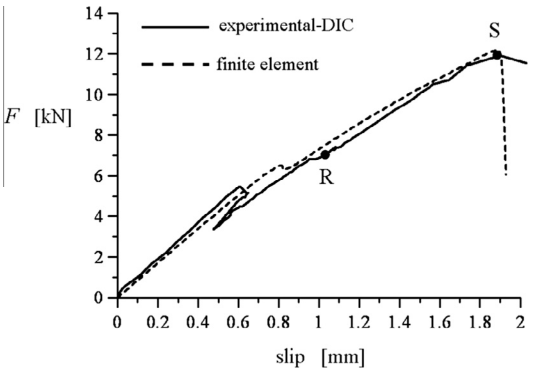

Fig. 13. Response of the single-lap shear test in terms of overall reaction force F as a function of the 'actual' tangential slip reconstructed through DIC (thick line), and its counterpart computed by means of the finite element analysis (dashed line). In the simulations the actual slip is prescribed as boundary condition to the CFRP free end, whilst rigid body motions of the pillar are prevented by ideal constraints.

machine frame, the relative slip was approximated by displacements in the upper part of the masonry support, estimated by DIC over two regions symmetrically located with respect to the reinforcement and then averaged. Such displacement history was prescribed as boundary condition to the finite element model (at the reinforcement free end), whilst rigid body motions of the modeled pillar are prevented by ideal (i.e. non-compliant) constraints. Explicit finite element simulations of single-lap experiment are therefore slip-driven. In Fig. 13, the reaction force provided by the load cell as a function of the reconstructed slip appears in a rather satisfactory agreement with its computed counterpart, which does not include the wedge crack occurred inside the last brick. The experimental plot still exhibits a pronounced snap-back phenomenon, and the final collapse appears less brittle than in the numerical predictions.

Fig. 14 shows the tangential relative displacement between the CFRP strip and the masonry support detected by DIC, and the relevant field computed by the finite element model at the same values of the reaction force. The region-of-interest (ROI) where the analysis was carried out is shown in Fig. 14. Also in this case, the agreement is really important. The availability of full-field measurements has allowed us to assess the mechanical model also in terms of local deformation.

5. Closing remarks and future prospects

In this paper, a methodology was proposed to investigate the delamination phenomena between a CFRP strip and masonry during single-lap shear tests. The tested pillar was composed of three historical clay bricks from a XVII century rural building, bonded by two thick joints of high-strength mortar, recently proposed for restoration interventions. A complex system, including several independent parts and connections (stiffened frame, bolted plates, connecting rods, etc.), was realized to generate tangential slips between the reinforcement and the support, while reducing as much as possible rigid-body motions under high loading.

Experimental data gathered from different sources during the test were discussed and compared with the results of advanced computer simulations, namely: (i) conventional data, as the overall reaction force and the actuator stroke; (ii) relative displacement components between the CFRP strip and the support, provided by contact point sensors, namely by two LVDTs and a clip gauge located closely to the notch and at the strip attachment, respectively; (iii) no-contact, kinematic full-field measurements provided by 2D (plane) Digital Image Correlation (2D DIC), processing single-camera digital images of the specimen reinforced surface.

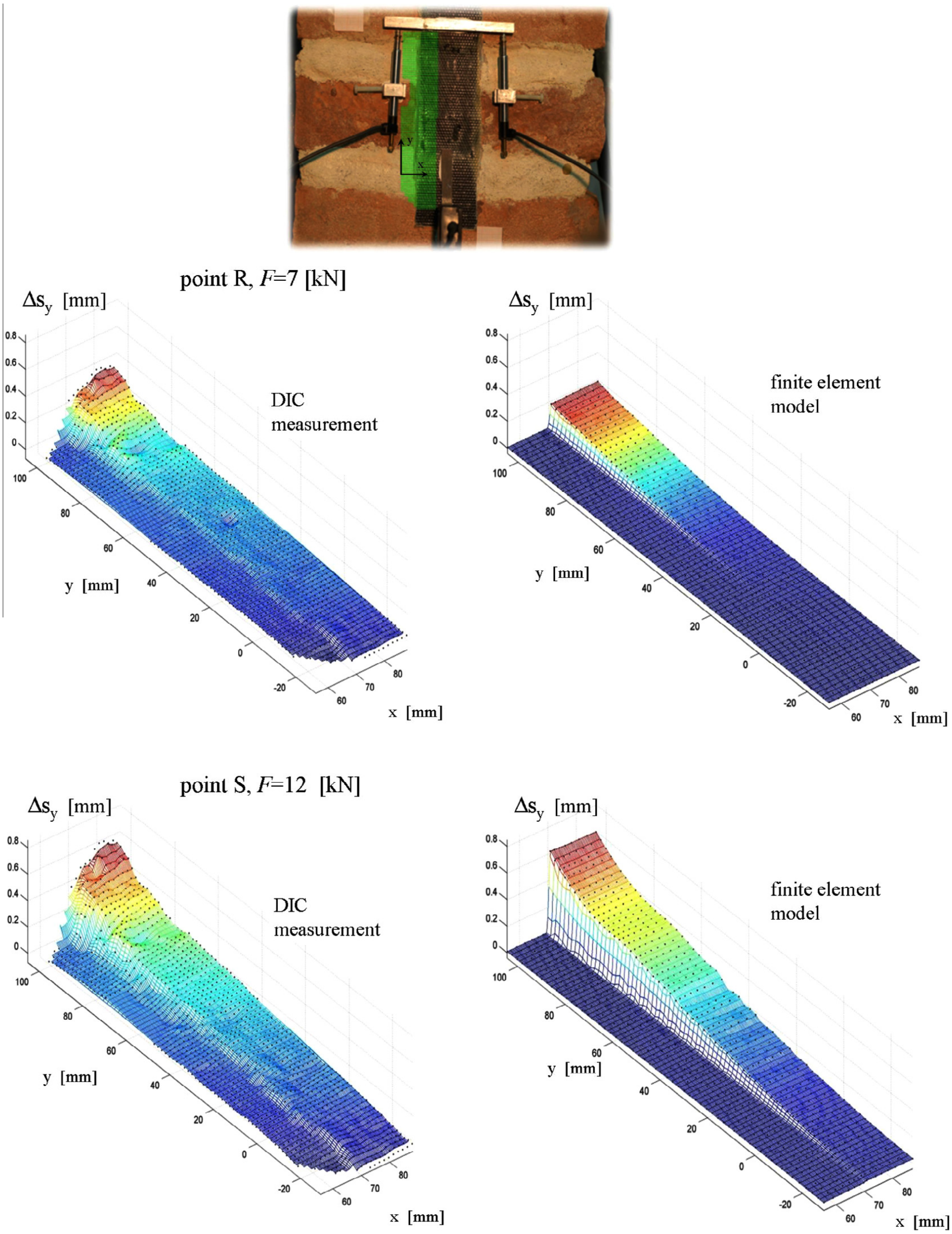
point R, F=7 [kN]

point S, F=12 [kN]

Fig. 14. Relative tangential displacements between the CFRP reinforcement and the masonry support, estimated by 2D DIC at different loading phases during the shear test (points labeled as R and S are indicated in Fig. 13), and their counterparts computed by the finite element model. The upper picture shows the wide field-of-view covered by the camera, and the ROI (green-colored) selected for these analyses. (For interpretation of the references to color in this figure legend, the reader is referred to the web version of this article.)

The proposed strategy exhibits several novel features: (i) the clip gauge, located at the anchorage of the reinforcement strip, allowed for the stable control of the test up to complete debonding of CFRP strip from the support; (ii) due to the large field-of-view and high resolution images, 2D DIC procedure was applied to detect accurately the in-plane displacements of the whole monitored surface, not only in the neighborhood of the CFRP reinforcement; (iii) rigorous mathematical models were adopted to describe camera lens distortions and transformation of points tracked with DIC from image space to metric object space; (iv) accuracy and resolution of the adopted optical system were validated with independent benchmarking tests. Furthermore, kinematic data were used to estimate the Young elastic modulus of the CFRP reinforcement after the preparation process (implying the superposition of several layers of adhesive and grout, or 'stucco'), and to reconstruct the 'actual' boundary conditions prescribed to the specimen. In fact, the evolution of overall tangential slips during the experiment (performed under clip gauge control) could not be predicted on the basis of usually available data, and in this case it was reconstructed through DIC.

The three-dimensional finite element model of the tested pillar, taking into account the single masonry constituents, was developed under the simplifying hypothesis of perfect adhesion between the CFRP reinforcement and the support. This model predicted bulk damage inside the specimen, correlating it to the macroscopic response and to surface measurements. The deformation scenario was confirmed by post-mortem inspection of the detached CFRP strip: this reported some material extracted from the support, markedly thicker over the inner brick and almost negligible over the mortar joints. An excellent agreement was found also for the relative displacements between CFRP and masonry, detected by DIC closely to the reinforcement, and those computed by the numerical model at the same values of the overall reaction force.

The presence during the experiment of unstable crack propagation phases along the reinforcement–masonry interface suggests a viable route to improve the predictive capabilities of the finite element model. In particular, interface damage along the FRP–masonry joint allowing for kinematic discontinuities could be introduced, and coupled effectively with the bulk mechanisms. Moreover, clip control could be implemented for the explicit finite element simulations.

This study confirms that complementary experimental information, such as the overall reaction force and actuator stroke, conventional point sensors and no-contact measurements, can be extremely useful to correctly interpret the mechanical response of heterogeneous samples subjected to non-trivial tests. In particular, 2D DIC can play a crucial role in order to monitor the actual boundary conditions prescribed to the specimen during laboratory tests, as a basis to calibrate advanced finite element models. The adopted numerical tool, if properly calibrated and validated, is expected to accurately predict the response of reinforced masonry elements under conditions which are difficult to recreate in the laboratory (e.g., earthquakes). Moreover, it gives an important feedback to select the optimal retrofitting interventions and the most suitable restoration materials.

Acknowledgements

The Authors kindly acknowledge the support provided by the Department of Structural Engineering at Politecnico di Milano in the framework of the Young Research Fund 2010. The authors wish to extend their gratitude to Prof. Sara Cattaneo and Dr. Paola Condoleo, Dr. Fabio Roncoroni, Eng. Raffaele Bazzi and Eng. Enrico Moroni for various helps concerning the experimental program. Mapei Spa provided assistance for the experiments. This research partially benefited from the support of the FIRB 2011 National Research Program (D.D. 9th November 2011, n. 928). Acknowledgements also go to the Basic National Research Program of China (No. 2013CB733204).

References

[1] Abaqus. Release 6.10-1. Theory and user's manuals. Hibbit, Karlsson and Sorensen Inc.: Pawtucket, RI, USA; 2010.

[2] Barazzetti L, Scaioni M. Crack measurement: development, testing and applications of an automatic image-based algorithm. ISPRS J Photogramm Remote Sens 2009;64(3):285–96.

[3] Barazzetti L, Scaioni M. Development and implementation of image-based algorithms for measurement of deformations in material testing. Sensors 2010;10:7469–95.

[4] Binda L, Tiraboschi C, Mirabella Roberti G, Baronio G, Cardani G. Measuring masonry material properties: detailed results from an extensive experimental research. Part I 'Tests on masonry components', National Research Council (CNR) and National Group for the Defence against Earthquakes (GNDT). Report 5.1 (CD-ROM), Politecnico di Milano, Milano; 1996.

[5] Biolzi L, Ghittoni C, Fedele R, Rosati G. Experimental and theoretical issues in FRP-concrete bonding. Constr Build Mater 2013;41(c):182–90. doi: 10.1016/j.conbuildmat.2012.11.082.

[6] Comi C, Perego U. Fracture energy based bi-dissipative damage model for concrete. Int J Solids Struct 2001;38:6427–54.

[7] Comi C, Fedele R, Perego U. A chemo–thermo-damage model for the analysis of concrete dams affected by alkali–silica reaction. Mech Mater 2009;41:210–30.

[8] CNR DT-200 R1. Guide for the design and construction of externally bonded FRP systems for strengthening existing structures. National Research Council (CNR), Rome, Italy; 2012.

[9] Fedele R, Milani G. A numerical insight into the response of masonry columns reinforced by FRP strips: the case of perfect adhesion. Compos Struct 2010;92(10):2345–57.

[10] Fedele R, Milani G. Assessment of bonding stresses between FRP sheets and masonry pillars during delamination tests. Composites Part B 2012;43:1999–2011.

[11] Fedele R, Raka B, Hild F, Roux S. Identification of adhesive properties in GLARE laminates by digital image correlation. J Mech Phys Solids 2009;57(7):1003–16.

[12] Ferretti D, Freddi F, Rosati G, Rossi M. Snap-back shear tests of FRP plates bonded to concrete. Eng Fract Mech 2011;78(15):2663–78.

[13] Fraser CS. Photogrammetric measurement to one part in a million. Photogramm Eng Remote Sens 1992;58:305–10.

[14] Fraser CS. Automatic camera calibration in close range photogrammetry. Photogramm Eng Remote Sens 2013;79:381–8.

[15] Grün A. Development and status of image matching in photogrammetry. Photogramm Rec 2012;27(137):36–57.

[16] Kraus K. Photogrammetry, vol. 2. Bonn: Dümmler Verlag; 1997.

[17] Luhmann T, Robson S, Kyle S, Harley I. Close range photogrammetry: principles, techniques and applications. Dunbeath, Caithness, Scotland, UK: Whittles Publishing; 2011.

[18] Maas H-G, Hampel U. Photogrammetric techniques in civil engineering material testing and structure monitoring. Photogramm Eng Remote Sens 2006;72(1):39–45.

[19] Subramaniam KV, Focacci F, Carloni C. An investigation on the interface fracture propagation between FRP and masonry. In: Proc MuRiCo 3, mechanics of masonry structures strengthened with composite materials: modeling, testing, design, control. Venice, Italy; April 2009.